Texture analysis of ultrasound images obtained with different beamforming techniques and dynamic ranges – a robustness study

Ultrasonics 131 (2023) 106940

Contents lists available at ScienceDirect

Ultrasonics

journal homepage: www.elsevier.com/locate/ultras

Texture analysis of ultrasound images obtained with different beamforming techniques and dynamic ranges – A robustness study

Silvia Seoni [a,*], Giulia Matrone [b], Kristen M. Meiburger [a]

[a] Polito[BIO]Med Lab, Biolab, Dept. of Electronics and Telecommunications, Politecnico di Torino, Torino, Italy
[b] Dept. of Electrical, Computer and Biomedical Engineering, University of Pavia, Pavia, Italy

ARTICLE INFO

Keywords:
Texture analysis
Ultrasound image dynamic range
Ultrasound beamforming
Robustness analysis

ABSTRACT

Texture analysis of medical images gives quantitative information about the tissue characterization for possible pathology discrimination. Ultrasound B-mode images are generated through a process called beamforming. Then, to obtain the final 8-bit image, the dynamic range value must be set. It is currently unknown how different beamforming techniques or dynamic range values may alter the final image texture. We provide here a robustness analysis of first and higher order texture features using six beamforming methods and seven dynamic range values, on experimental phantom and *in vivo* musculoskeletal images acquired using two different ultrasound research scanners. To investigate the repeatability of the texture parameters, we applied the multivariate analysis of variance (MANOVA) and estimated the intraclass correlation coefficient (ICC) on the texture features calculated on the B-mode images created with different beamforming methods and dynamic range values. We demonstrated the high repeatability of texture features when varying the dynamic range and showed texture features can differentiate between beamforming methods through a MANOVA analysis, hinting at the potential future clinical application of specific beamformers.

1. Introduction

Ultrasound imaging has proven to be effective in the investigation of organs, tissue functionality and health [1,2]. The ultrasound image shows a unique speckle pattern, also called image texture, which results from the interaction between tissue components and the ultrasonic wave.

Texture analysis of medical images gives quantitative information about the tissue characterization and internal structure of organs for possible pathology discrimination. Indeed, texture features have shown to be informative in the characterization of various tissues, such as muscles [3], ovarian tumors [4], and thyroid lesions [5]. Quantitative texture features are typically divided into first-order and higher-order texture features [3]. Among first-order ones, a commonly used and very simple texture feature is the gray scale mean, which has been used to differentiate between healthy and pathological or fatigued tissues [6]. However, it is highly dependent on the image intensity histogram and hence also on the image acquisition settings. On the other hand, higher-order texture features are robust to image intensity levels, being intensity invariant [7] and analyzing not the actual pixel intensity values but the patterns that emerge between adjacent pixels. There are numerous higher-order texture features that have been employed for ultrasound image analysis; some of the most common include the Haralick features, Galloway features, local binary patterns (LBP), and the fractal dimension (FD) [8–11]. The Haralick and Galloway features are based on computing a feature matrix (i.e., gray-level co-occurrence matrix (GLCM) and run length matrix (RLM), respectively) whose dimensions are determined by the number of gray levels that are considered in the image, a process that is called quantization. The resulting features hence depend on the quantization step that is employed and are reproducible when the same quantization is performed. Löfstedt et al. [12] recently proposed gray-level invariant Haralick texture features by redefining the GLCM as a discretized probability density function, producing texture feature values independent of the image quantization. The computation of LBP does not require image quantization. As such, these features are more robust to image gray levels, and studies have demonstrated how two powerful descriptors are the energy and entropy of the LBP distributions [13]. There are several studies in the literature using LBP and FD as estimators for the classification of pathological tissues or organs, such as thyroid [14,15] or breast [16] lesions.

Quantitative texture features are computed on the ultrasound B-mode image, which is formed through a process called beamforming.

* Corresponding author.
E-mail address: silvia.seoni@polito.it (S. Seoni).

https://doi.org/10.1016/j.ultras.2023.106940
Received 27 March 2022; Received in revised form 26 January 2023; Accepted 29 January 2023
Available online 1 February 2023

When considering focused wave imaging, beamforming combines the raw signals that arrive at the ultrasound transducer elements during reception usually to generate one image scan line as a combination of them, and the final image is produced by the repetition of this process line-by-line. Then the B-mode image can be generated after envelope extraction, normalization and logarithmic compression [17]. Numerous beamforming methods for ultrasound imaging have been presented and studied [17,18] providing a better image resolution and contrast when compared to the conventional delay-and-sum (DAS) technique [19–21]. Recently, deep neural networks (DNNs) have also been proposed for beamforming and segmentation [22–25].

Different beamforming methods may alter the obtained ultrasound B-mode image and hence the image texture. While there are many studies proposing innovative beamforming techniques, their influence on the output B-mode image texture is still unknown.

Furthermore, the quantitative analysis of B-mode images may vary depending on ultrasound setting parameters. Dynamic range is defined as the difference between the maximum and minimum values of the displayed signal. The value of dynamic range influences image visualization, so its possible influence on texture parameters should be investigated. Time-gain compensation (TGC) and dynamic range are the two parameters that are most often modified to improve image visualization. Some studies have shown the influence of TGC and dynamic range on the quantitative analysis of the ultrasonographic images [26,27], showing how TGC appears to heavily influence most of the texture features while changing the dynamic range has no significant effect on them. Although the value of the dynamic range does not seem to influence the texture parameters, a closer study could investigate the influence the dynamic range may have as the beamforming method used to form the image changes. Indeed, adaptive and non-linear beamformers may alter the image dynamic range [28,29]. Thus, using the same standard dynamic range (for example, 60 dB) for displaying images reconstructed by different beamforming techniques produces B-mode images that are visually quite different. An automatic method was presented in [30] to adjust the dynamic range of the B-mode image to get similar brightness and contrast of a predetermined reference image. An automatic method to estimate the optimal dynamic range was presented also in [31], that matches the histograms of images obtained with various beamformers. Histogram matching was also proposed in [32] and [33] to qualitatively compare images obtained with DAS and different coherence-based beamformers, and was further analysed in [34,35].

It is thus crucial to understand if quantitative texture features are robust among different beamformers and dynamic ranges used for the final image display. In this study, we expand upon our previous work [36], in which we analysed the robustness of the first and second order texture features estimated on a phantom and *in vivo* vastus lateralis muscle images experimentally acquired using the ULA-OP research scanner [37] and reconstructed with six different beamforming methods. Here, we have extended the previous study [36] by including:

- additional texture features in our analyses, now considering also LBP and the FD;
- a multi-device analysis, comprehending results from images acquired with two independent research scanners, making the obtained results more generalizable and applicable;
- a multi-muscle, multi-phantom analysis, including images experimentally acquired on two different muscles and phantoms.

In this way, we have provided a more in-depth investigation of how texture features may change when different shapes and/or sizes of regions of interest (ROIs) are selected for feature calculation, and when different dynamic range values and different beamforming methods are employed to reconstruct the image.

2. Materials and methods

2.1. Acquisition of phantom and in vivo ultrasound images

The dataset used for the analyses consists of phantom images and *in vivo* muscle images, acquired using two different devices: the ULA-OP [37] and the Verasonics Vantage™ research ultrasound systems. The ULA-OP dataset consists of two phantom images (model 040GSE, CIRS Inc, USA) containing point-like reflectors and a hyperechoic structure (Fig. 1A) or an anechoic structure (Fig. 1B), and 8 *in vivo* transversal musculoskeletal images of the gastrocnemius (4 images, Fig. 1C) and vastus lateralis (4 images, Fig. 1D) muscles acquired on a healthy volunteer. The Verasonics dataset consists of three phantom images (model 054GS, CIRS Inc, USA) containing point-like reflectors and a hyperechoic structure or an anechoic structure, and 4 *in vivo* transversal musculoskeletal images of the gastrocnemius (2 images) and vastus lateralis (2 images) acquired on one healthy subject.

The ULA-OP images were acquired using a 192-element linear array probe (model LA533, Esaote s.p.a., Florence, Italy) at 7 MHz central frequency. Both in transmission and reception, a 64-element aperture was used. The transmitted signal was a 2-cycle, Hanning-tapered sinusoidal burst at the central frequency mentioned. During the acquisitions, the transmit focal depth was set to 15 mm, 30 mm, and 25 mm, for the phantom image with a hyperechoic structure, the phantom image with an anechoic structure, and the *in vivo* images, respectively. Dynamic focusing was always applied in reception considering a F-number F#=2 and applying a Hann apodization window; 192 scan lines were acquired. The Verasonics images were acquired using a 128-element linear array probe (model *L*11-5v) at 7 MHz central frequency. Both in transmission and reception, a 64-element aperture was used. The transmitted signal was a 2-cycle, Hanning-tapered sinusoidal burst at the central frequency mentioned. During the acquisitions, the transmit focal depth was set to 38 mm and 25 mm, for the phantom image and for the *in vivo* images, respectively. 128 scan-lines were acquired and image reconstruction was performed applying the same settings as those described for the ULA-OP system.

The raw radiofrequency (RF) signals (i.e. pre-beamforming signals) were processed in Matlab (The MathWorks, Natick, MA, USA). Starting with the same RF datasets, we generated six B-mode images using the different beamforming methods that are briefly described in the next section. A more comprehensive overview of the beamforming techniques can be found in [17] and [38].

2.2. Beamforming methods and automatic dynamic range

The DAS algorithm focuses the received beam by applying geometrically computed delays to the signals coming from the N elements of the active aperture of the transducer array. The sum of all aligned RF signals $s_i(t)$ generates the beamformed RF signal $y_{DAS}(t)$, which is used to generate one scan line of the final B-mode image in a line-by-line process:

$$y_{DAS}(t) = \widehat{s}_i(t-\tau_i) = \sum_{i=1}^{N} s_i(t). \quad (1)$$

Similar to DAS, the Filtered-Delay Multiply and Sum (F-DMAS) algorithm applies a delay to align the RF signals [17]. Unlike DAS, in which the signals are simply aligned and summed, in the F-DMAS algorithm, the focused signals are first coupled and multiplied. The square root is then applied to the absolute values and the sign is preserved. At this point, the signals are summed and then filtered with a band-pass filter. The DAS output shows an amplitude spectrum comparable to that of raw signals. Instead, both the baseband (DC or 0 Hz) and second harmonic component are presented in the spectrum of the F-DMAS beamformed signal. Thus, the band-pass filter (*BPfilter*) filters the F-DMAS signals to remove the DC and higher frequency components,

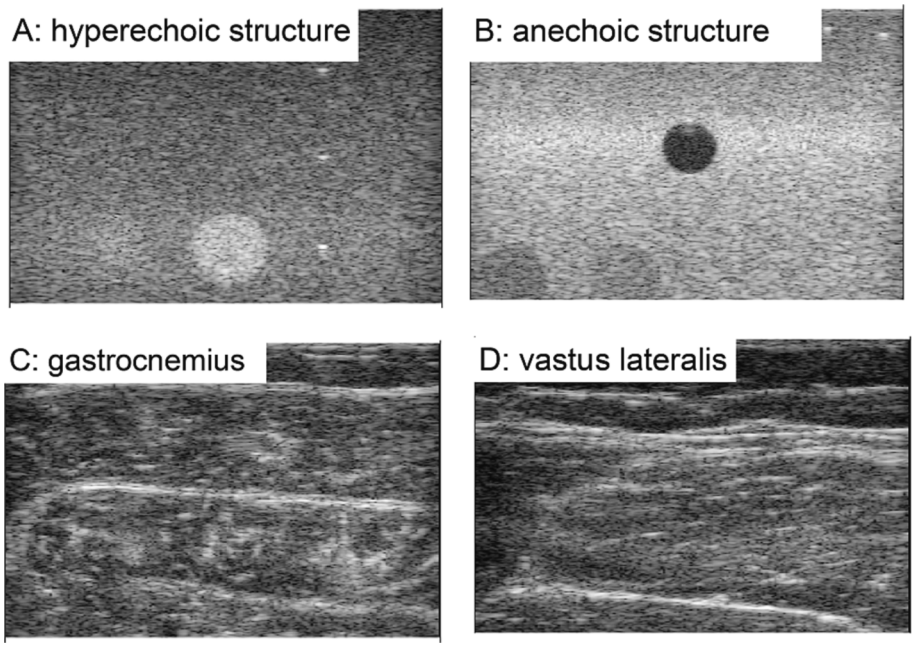

Fig. 1. The first row shows an example of a phantom image containing point-like reflectors and a hyperechoic structure (A) and an anechoic structure (B). The second row shows an example of the *in vivo* musculoskeletal images: gastrocnemius (C) and vastus lateralis (D) muscles. The four images are from the ULA-OP dataset.

allowing only the second harmonics to pass:

$$y_{FDMAS} = BPfilter\left\{ \sum_{i=1}^{N-1} \sum_{j=i+1}^{N} sign\left(s_i(t)s_j(t)\right) \cdot \sqrt{\left|s_i(t)s_j(t)\right|} \right\} \tag{2}$$

The other implemented beamforming algorithms were the coherence factor (CF) [39], generalized CF (GCF) [18], phase and sign CF (PCF and SCF, respectively) [40]. These methods apply a weighting matrix to the DAS-beamformed image, computed in the following way:

$$y_{CF}(t) = y_{DAS}(t) \cdot CF(t) = y_{DAS}(t) \cdot \frac{\left|\sum_{i=1}^{N} s_i(t)\right|^2}{N\sum_{i=1}^{N} |s_i(t)|^2} \tag{3}$$

$$y_{GCF}(t) = y_{DAS}(t) \cdot GCF(t) = y_{DAS}(t) \cdot \frac{\sum_{k=1}^{M_0} |S(k,t)|^2}{\sum_{k=0}^{N-1} |S(k,t)|^2} \tag{4}$$

$$y_{PCF}(t) = y_{DAS}(t) \cdot PCF(t) = y_{DAS}(t) \cdot max\left\{0, 1 - \frac{\gamma}{\sigma_0}\sigma(\varphi(t))\right\} \tag{5}$$

$$y_{SCF}(t) = y_{DAS}(t) \cdot SCF(t) = y_{DAS}(t) \cdot |1 - \sigma(b_i(t))|^p \tag{6}$$

where k represents the spatial frequency index, $S(k,t)$ is the spectrum of s_i, M_0 is a spatial frequency threshold, γ and p are two user-defined parameters that can be employed to tune the sensitivity of PCF and SCF, respectively. $\sigma(\varphi_i)$ is the standard deviation of the signals instan-

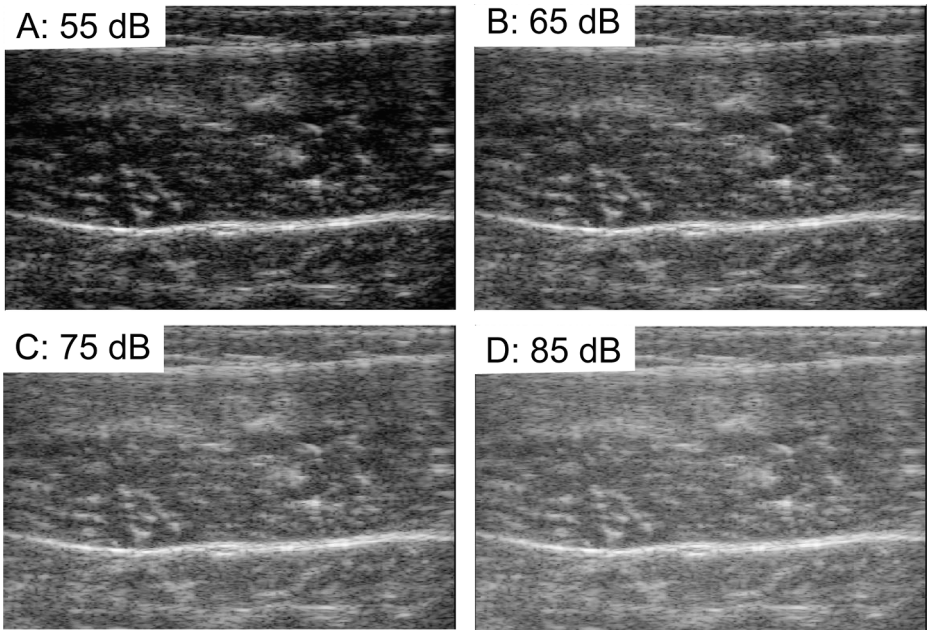

Fig. 2. An example of the different dR values for the creation of final gray-level DAS gastrocnemius muscle images (ULA-OP dataset).

taneous phases φ_i, and $b_i(t) = sign(s_i)$.

Both for the phantom images and for *in vivo* images, we varied the M_0 value in the range 1–5, and γ and p in the range 0.2–1 with a step of 0.2.

After beamforming of the RF signals and envelope detection, the image is normalized by its maximum value and log-compressed. To obtain the final 8-bit pixel image, we used a threshold of -dR (dB) to cut-off the values out of the selected dynamic range (i.e., [-dR; 0] dB) and we converted the pixel values into a range 0–255. Then, a calibration factor of 0.06 mm/pixel, a common value in medical ultrasound images, was used to interpolate and scale the final pixel image in both directions (i.e., in ULA-OP dataset, a raw data input image of 2048 × 192 pixels that was scanned over 31.5 × 46.8 mm had final dimension of 525 × 779 pixels, along the z axis and x axis, respectively). Fig. 2 displays the same gastrocnemius muscle image obtained with different dynamic ranges, showing how this parameter can greatly influence the output image visualization.

Furthermore, an automatic dR value was computed to obtain visually similar images for all beamforming methods following the procedure described in [31]. Fig. 3 shows an example of how the automatic dR makes the images qualitatively more similar even if they were generated using different beamforming techniques.

2.3. Texture analysis

A quantitative texture analysis was done on the 8-bit B-mode images varying six beamforming methods and seven dR values. Four regions of interest (ROIs) were manually placed on the phantom images, to consider ROIs including a uniform hyperechoic region (ROI_1 in Fig. 4 (B)), a reflector (ROI_2 in Fig. 4(B)), both an anechoic and a uniform area of the image (ROI_3 in Fig. 4(D)), and a uniform speckle region (ROI_4 in Fig. 4(D)).

In the *in vivo* musculoskeletal images, a single ROI was placed between the aponeuroses. An example of ROI selection is displayed in Fig. 4A for the gastrocnemius muscle and in Fig. 4C for the vastus lateralis muscle. A total of 52 texture features were computed within the ROIs on the obtained images, which are described in the following subsections.

The texture parameters were computed on the 8-bit image ROIs without normalizing the intensity values by the maximum value within the ROI. In fact, normalization would influence only the values of the first-order texture parameters that depend on the image intensity histogram. Since the majority of the considered texture features are higher-order, as described in the next sections, we empirically chose to not normalize the pixel intensity values.

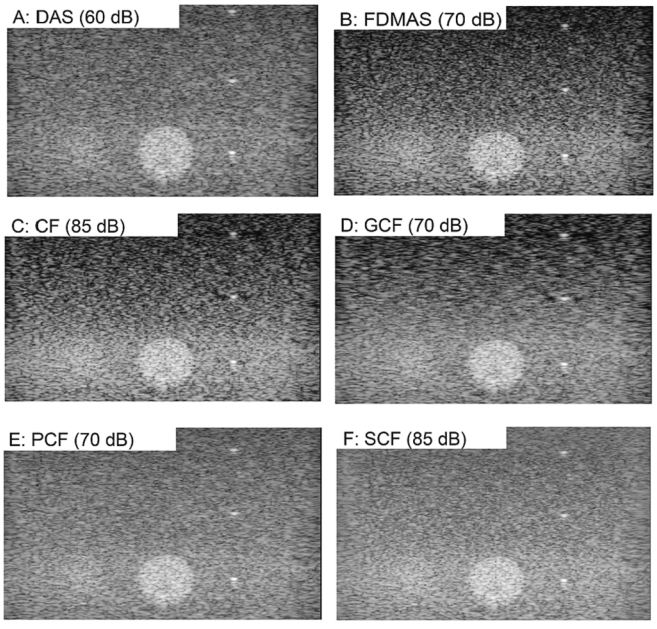

Fig. 3. A phantom image (ULA-OP dataset) obtained with different beamforming techniques and displayed using the automatically determined dR (shown in brackets).

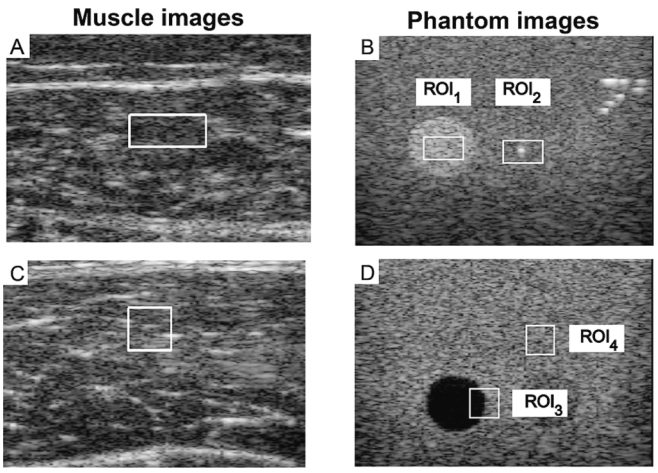

Fig. 4. An example of two different shapes and dimensions of ROIs (one for the muscles and four for the phantom) placed on the muscle (A, C) and phantom (B, D) images. The images are displayed using the automatic dynamic range and beamformed with DAS. The images are from the Verasonics dataset.

2.3.1. First-order features

The first-order texture features are indicators of the image intensity histogram. Table 1 shows the mathematical description of the estimated features: mean, variance, skewness, kurtosis, and entropy.

2.3.2. Higher-order texture features

Higher-order texture features are intensity invariant and analyse whether specific patterns between pixel intensity values can be extracted. The Haralick features are based on the GLCM [41] which is a square matrix that measures the number of times a specific intensity pattern between adjacent pixels is repeated, with a dimension equal to the number of the gray levels. The GLCM was computed using 32 gray levels, as this is a commonly used value for quantization, and the considered directions were equal to 0°, 45°, 90°, and 135°. Table 2 shows the mathematical description of the six Haralick texture features that were computed on the GLCM, considering the various directions, with a total of 24 Haralick features.

The Galloway features are mathematical descriptors of the RLM [11]. The RLM is a matrix in which each element represents the number of pixels with run length i and intensity j in a given direction. As for the

Table 1
Mathematical Description of First-Order Features.

Feature	Description
Mean (m)	$m = \sum_{x=1}^{M}\sum_{y=1}^{N}\frac{I(x,y)}{M\cdot N}$
Variance (σ^2)	$\sigma^2 = \frac{\sum_{x=1}^{M}\sum_{y=1}^{N}\{I(x,y)\text{-}m\}^2}{M\cdot N}$
Skewness (S_k)	$S_k = \frac{1}{M\cdot N}\frac{\sum_{x=1}^{M}\sum_{y=1}^{N}\{I(x,y)\text{-}m\}^3}{\sigma^3}$
Kurtosis (K_t)	$K_t = \frac{1}{M\cdot N}\frac{\sum_{x=1}^{M}\sum_{y=1}^{N}\{I(x,y)\text{-}m\}^4}{\sigma^4}$
Entropy (Ent_1)	$Ent_1 = -\sum_{p=1}^{Nhist} hist(p)\cdot\log_2(hist(p))$

$I(x,y)$ denotes the input ROI. M is the number of columns of the ROI. N is the number of rows of the ROI. Nhist is the number of gray levels of the histogram and hist(p) contains the normalized histogram counts of the image intensity histogram.

Table 2
Mathematical Description of Haralick Features and Galloway Features.

Haralick Feature	Description	Galloway Feature	Description
Symmetry (I_{sym})	$I_{sym} = 1\text{-}\sum_{i=0}^{N-1}\sum_{j=0}^{N-1}\lvert i\text{-}j\rvert P(i,j)$	*Short run emphasis (SRE)*	$SRE = \frac{\sum_{i=1}^{N_g}\sum_{j=1}^{N_r}\frac{R(i,j)}{j^2}}{\sum_{i=1}^{N_g}\sum_{j=1}^{N_r}R(i,j)}$
Contrast (I_{con})	$I_{con} = \sum_{n=0}^{N-1} n^2 \left\{\sum_{i=0}^{N-1}\sum_{j=0}^{N-1} P(i,j)\right\}$	*Long run emphasis (LRE)*	$LRE = \frac{\sum_{i=1}^{N_g}\sum_{j=1}^{N_r} j^2 R(i,j)}{\sum_{i=1}^{N_g}\sum_{j=1}^{N_r}R(i,j)}$
Homogeneity (I_{hmg})	$I_{hmg} = \left\{\sum_{i=0}^{N-1}\sum_{j=0}^{N-1}\frac{1}{1+(i-j)^2}P(i,j)\right\}$	*Gray-level nonuniformity (GLNU)*	$GLNU = \frac{\sum_{i=1}^{N_g}\left(\sum_{j=1}^{N_r}R(i,j)\right)^2}{\sum_{i=1}^{N_g}\sum_{j=1}^{N_r}R(i,j)}$
Entropy (I_{Entr})	$I_{Entr} = -\sum_{i=0}^{N-1}\sum_{j=0}^{N-1} P(i,j)\log P(i,j)$	*Run length nonuniformity (RLNU)*	$RLNU = \frac{\sum_{j=1}^{N_r}\left(\sum_{i=1}^{N_g}R(i,j)\right)^2}{\sum_{i=1}^{N_g}\sum_{j=1}^{N_r}R(i,j)}$
Correlation (I_{cor})	$I_{cor} = \frac{\sum_{i=0}^{N-1}\sum_{j=0}^{N-1}(i-j)P(i,j) - \mu_x,\mu_y}{\sigma_x \cdot \sigma_y}$	*Run percentage (RP)*	$RP = \frac{\sum_{i=1}^{N_g}\sum_{j=1}^{N_r}R(i,j)}{N_g\, N_r}$
Energy (I_{enrg})	$I_{enrg} = \sum_{i=0}^{N-1}\sum_{j=0}^{N-1}(P(i,\ j))^2$		

$P(i,j)$ is equal to $\frac{C(i,j)}{\Sigma C(i,j)}$, where $C(i,j)$ represents the GLCM. $\sigma_x,\ \sigma_y,\ \mu_x,\mu_y$ are the standard deviations and means of Px, Py, the marginal probability density functions. $R(i,j)$ denotes the run length matrix. N_g represents the number of gray values in the image (i.e., the number of rows of the matrix R), N_r represents the number of runs (i.e., the number of columns of the R matrix).

GLCMs, also the RLMs were computed using 32 gray levels. We estimated the Galloway features at the same 4 angles (i.e., 0°, 45°, 90° and 135°). The mathematical descriptions of the five Galloway features are shown in Table 2. Considering the four directions, a total of 20 Galloway features were computed for each ROI. For the computation of these texture features, a unitary interpixel distance was considered.

Then, the FD features and LBP features were estimated [8–10,42–45]. The FD describes an invariant representation of an image, which preserves the invariant shape even in the event of significant shrinkage or enlargement of image objects. It also represents the irregularity and roughness of pixel intensities. In addition, the LBP features were computed [8,9]. To define the LBP, the value of P, the number of pixels of the considered neighborhood, and R, the radius of the neighborhood, were set equal to 8 and 1 respectively [8,9]. In this way, a neighborhood of 8 pixels was considered to estimate the patterns. To formally define 'uniform' patterns, a uniformity measure U was used, which corresponds to the number of spatial transitions (between 0 and 1) in the pattern encoded by 0 and 1. The value of U was set equal to 2 so that all patterns that have at least three (2 + 1) spatial transitions were defined as uniform. From the LBP mask, the values of entropy and energy were estimated, which show lower values for more homogeneous images and higher values for inhomogeneous images.

Overall, a total of 52 texture parameters were computed for each ROI: 5 first-order parameters, 24 Haralick features, 20 Galloway features, 2 LBP features and the FD. Numerous studies compute an even larger number of features (e.g., hundreds of features), considering different interpixel distances (e.g., from 1 to 5) and then typically a feature selection technique is applied to maximize the discrimination capability of the texture features (e.g., between pathological and healthy images). This type of analysis is outside of the scope of this present study, hence here we limited the number of texture features to include the most representative features for ultrasound images that have been used in several previous studies [3,6,7,46].

2.4. Robustness analysis

We estimated the intraclass cross-correlation coefficient (ICC) and applied the multivariate analysis of variance (MANOVA) to provide a robustness analysis of the considered texture features. We estimated ICC 1–1 [47] which reflects the degree of correlation and agreement between measurements. In general, we considered ICC < 0.5 as an index that the texture features vary greatly among the different cases, 0.5 < ICC < 0.75 as moderate robustness of the texture features, 0.75 < ICC < 0.9 as good robustness, and ICC > 0.9 as excellent robustness. Briefly, the multivariate analysis of variance (MANOVA) takes a set of multiple continuous variables and groups them into a weighted linear combination. This analysis tests the null hypothesis that the mean values of each group are the same *n*-dimensional multivariate vector, and that any difference observed in the sample of the features is due to random chance. In this way, we could estimate the canonical variables, which represent a linear combination of the original features. We used the p-value and dimension (*d*) to determine whether the groups showed statistically significant differences. The *d* value is an estimate of the dimension of the space containing the group means, which has a range from 0 up to the number of considered groups minus one. If *d* is equal to zero, this implies that the considered groups cannot be effectively distinguished.

A series of analyses was carried out to evaluate how beamforming and the dynamic range may influence the texture features, as summarized in Table 3. In particular, the following analyses were done on the computed texture features:

Table 3
Analysis of the Texture Parameters on Phantom and Muscle Images.

Analysis	Description
A1	Estimation of the ICC values varying the shape and dimension of the ROIs
A2	Estimation of ICC values varying the values of M_0, γ, and p for GCF, PCF and SCF method respectively, using the automatic dR
A3	MANOVA analysis on the texture features computed on the muscle and phantom images together obtained with one beamforming method using the different dR values as the independent group (with $M_0 = 2$, $\gamma = 0.8$, and $p = 0.8$ for GCF, PCF and SCF method, respectively)
A4	MANOVA analysis on the texture features computed on the muscle and phantom images together obtained with the automatically computed dR values using the different beamforming methods as the independent group (with $M_0 = 2$, $\gamma = 0.8$, and $p = 0.8$ for GCF, PCF and SCF method, respectively)
A5	MANOVA analysis on the texture features computed on the images obtained with different beamforming methods using the dR values as the independent group (with $M_0 = 2$, $\gamma = 0.8$, and $p = 0.8$ for GCF, PCF and SCF method, respectively)
A6	MANOVA analysis on the texture features computed on the images obtained with different dR values using the different beamforming methods as the independent group (with $M_0 = 2$, $\gamma = 0.8$, and $p = 0.8$ for GCF, PCF and SCF method, respectively)

A1. ICC analysis varying the ROI shapes and dimensions
A2. ICC analysis varying the M_0, γ, p parameters for GCF, PCF and SCF beamforming methods, respectively, using automatic dR values
A3. MANOVA analysis on the texture features computed on the images obtained with one beamforming method using the different dR values as the independent group (considering phantom and muscle images together)
A4. MANOVA analysis on the texture features computed on the images obtained with the automatically computed dR values using the different beamforming methods as the independent group (considering phantom and muscle images together)
A5. MANOVA analysis on the texture features computed on the images obtained with different beamforming methods using the dR values as the independent group (considering phantom and muscle images separately)
A6. MANOVA analysis on the texture features computed on the images obtained with different dR values using the different beamforming methods as the independent group (considering phantom and muscle images separately)

For the **A1 analysis**, to evaluate the texture parameters when changing the ROI size, we selected four different shapes/dimensions of the four ROIs on the phantom image, by varying their shape (square and rectangular) and dimensions (i.e. 30 × 30, 40 × 40, 50 × 30, and 60 × 40 pixel^2). For each muscle image, the texture features were estimated on the ROIs, again varying their shape and dimensions (i.e. 40 × 30, 50 × 50, 70 × 70, and 120 × 50 pixel^2). Considering the need to include only the muscular tissue ignoring the aponeurosis in the manually placed ROIs, it was necessary to limit the maximum ROI dimension to 120 × 50 pixel^2. ROIs were selected in a similar way both in the ULA-OP and Verasonics images.

For the **A2 analysis**, both for the phantom images and *in vivo* images, we varied the M_0 value in the range 1–5, and γ and p in the range 0.2–1 with a step size of 0.2.

The dynamic range values included seven different dR values in the range 55–85 dB with a step size of 5 dB. The beamforming methods that were analysed included the 6 methods that were previously described, specifically DAS, F-DMAS, CF, GCF, PCF, SCF. In A3-A6, $M_0 = 2$, $\gamma = 0.8$, and $p = 0.8$ were used for the GCF, PCF and SCF beamformers, respectively.

The ICC values in A1 and A2 were estimated for the ULA-OP dataset only, the Verasonics dataset only, and the total dataset composed of the ULA-OP and Verasonics datasets together. The MANOVA analyses were carried out on the total (ULA-OP + Verasonics) dataset, considering phantom and muscle images together (A3, A4) or separately (A5, A6).

3. Results

3.1. Robustness analysis – ROI characteristics and beamforming parameters

The first **analysis (A1)** was done to evaluate the influence of the shape and dimension of the ROIs on the texture parameters when estimated on the homogenous areas (hyperechoic and uniform regions, like ROI_1 and ROI_4 in Fig. 4B and 4D, respectively) and on the regions with mixed echogenicity (the reflector and the anechoic-uniform region, like ROI_2 and ROI_3 in Fig. 4B and 4D, respectively), using the seven values of dynamic range (55–85 dB) and the six beamformers, with varying M_0, γ and p parameters for the GCF, PCF, and SCF images, respectively. Table 4 shows the ICC results (the values reported in the text henceforth refer to the total dataset results), which indicate a high robustness of texture features for the homogenous ROIs (0.87) and a moderate robustness for the mixed intensity ROIs (0.72). The features estimated in the uniform ROIs show greater robustness than in the mixed ROIs when the size and shape of the ROI is varied. Based on these results, all further analyses were done employing the features computed within a fixed-size (i.e. 50 × 30 pixel^2) ROI. The final size was chosen empirically.

Table 4
Analysis A1: ICC Values Computed when Varying the ROI Size and Dimensions.

Dataset	Phantom *Homogeneous*	Phantom *Mixed*	Muscle *Gastrocnemius*	Muscle *Vastus Lateralis*
ULA-OP	0.88	0.72	0.73	0.73
Verasonics	0.86	0.70	0.73	0.77
Total dataset	**0.87**	**0.72**	**0.73**	**0.74**

The ICC values for the phantom and muscles images among the different ROIs shapes and dimensions. Values are shown for the phantom image homogeneous and mixed ROIs and for muscle image ROIs (gastrocnemius and vastus lateralis). In the table, the first row shows the ICC values for the ULA-OP dataset, the second for the Verasonics dataset and the last row for the total dataset, composed by the ULA-OP dataset and Verasonics dataset together (in bold).

For the *in vivo* study, we analysed separately the texture of the gastrocnemius and of the vastus lateralis muscle images. In analysis A1, the ICC values were similar in the two muscle image types, showing moderate robustness of the texture features (ICC = 0.73 and 0.74 for the gastrocnemius and vastus lateralis, respectively; see Table 4). All further analyses considered only ROIs with the same size (i.e. 70 × 70 pixel^2). The size of the final ROI was chosen empirically.

We then analysed the robustness of the texture features estimated on a specific ROI placed on the GCF, PCF and SCF images varying their specific parameters (M_0, γ and p), using the automatic dR values (**analysis A2**). In the phantom images, the results indicate excellent reliability of the texture features when varying these parameters, with ICC = 0.95 in GCF images and 0.99 in PCF and SCF images for the homogeneous regions (Fig. 5 (A)), and ICC = 0.63, 0.74 and 0.75 for the mixed ROIs (Fig. 5 (B)), when using the GCF, PCF and SCF methods, respectively. In the *in vivo* muscle images, the results indicate excellent reliability of the texture features when varying these parameters (ICC = 0.93 for the gastrocnemius muscle, and ICC = 0.96 for the vastus lateralis muscle, when considering the total dataset). The ICC values are shown in Fig. 5 (Fig. 5 (C), (D)). For all further analyses only one parameter value was selected for each beamformer, i.e. $M_0 = 2$, $\gamma = p = 0.8$.

For **analysis A3**, six different MANOVA analyses were done: in particular, the MANOVA was applied on the texture features computed on the muscle and phantom images together obtained with each single beamforming method and using the different dR values as the independent group (with $M_0 = 2$, $\gamma = 0.8$, and $p = 0.8$ for GCF, PCF and SCF method, respectively). In all 6 cases, hence considering each beamforming method independently, the parameter d was equal to zero.

When employing a MANOVA analysis on the texture features computed on the muscle and phantom images obtained with the automatically determined dR values and using the beamforming method as the independent group (**analysis A4**), the parameter d was instead equal to 5. Fig. 6 shows the first and second canonical variables of the MANOVA analysis.

3.2. Phantom images texture parameter analysis – Dynamic range and beamforming methods

Considering the MANOVA analysis, the features estimated on the images obtained with different beamforming methods using the dR values as the independent group showed a value of d equal to zero, which indicated that there are no significant differences between the groups (**analysis A5**). The scatter plots of the first and second canonical variables are displayed in Fig. 7 (A), (B). Through the MANOVA analysis, the coefficients of the new linear combination were estimated and we found the four features for each type of ROI that had the highest coefficients (in absolute value) for the first canonical variable, which are reported in Table 5. Furthermore, we applied the MANOVA on the

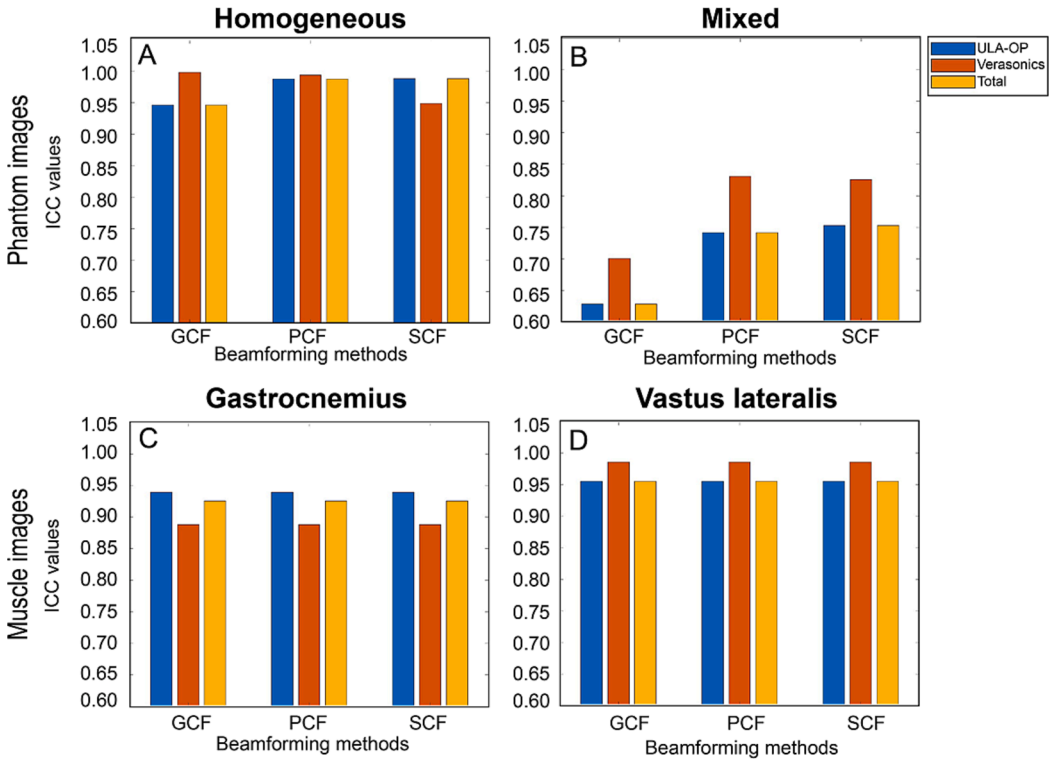

Fig. 5. The ICC values among the different values of M_0, γ, and p for GCF, PCF and SCF method respectively, using the automatic dR values (analysis A2). The top row shows the ICC values estimated in the phantom images ((A) homogeneous and (B) mixed ROIs), while the bottom row displays the ICC values estimated in muscle images ((C) gastrocnemius and (D) vastus lateralis ROIs).

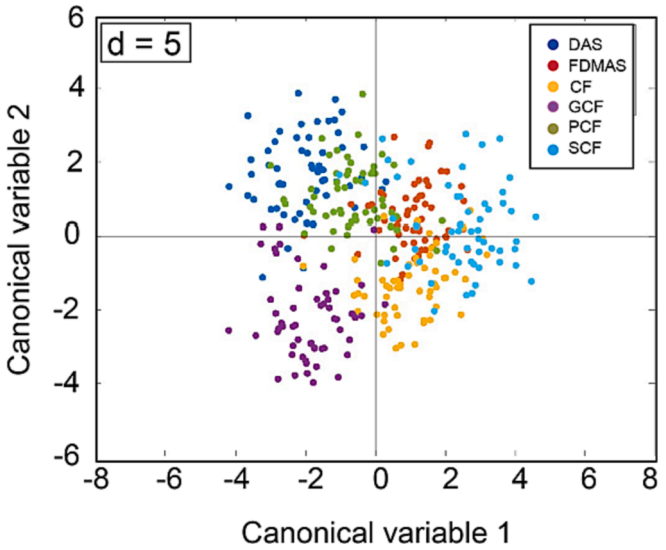

Fig. 6. The first and second canonical variables of texture features of the phantom and *in vivo* muscles images considering the different beamforming methods as the independent group and applying automatic dR values (analysis A4). The MANOVA analysis was applied on the texture features estimated on the two ROIs of the phantom images (homogeneous and mixed regions) and on the ROIs of the gastrocnemius and vastus lateralis images.

texture features obtained with the different dR values using the beamforming method as the independent group (**analysis A6**). The first and second canonical variables are displayed in Fig. 7 (C), (D). The MANOVA results show d equal to 5, demonstrating how the different beamforming methods can be distinguished. Table 6 reports the four features with the highest first canonical variable coefficient values for both types of ROIs when varying the beamforming method. In general, correlation, contrast, RP and SRE are the highest discriminant features among the different beamforming methods.

3.3. *In vivo muscle images texture parameter analysis – Dynamic range and beamforming methods*

Regarding *in vivo* images, the texture features estimated on images obtained with different beamforming methods using the dR values as the independent group (**analysis A5**) showed a value of d equal to zero with the MANOVA analysis, for both the gastrocnemius and vastus lateralis muscles. Table 5 reports the four features with the highest coefficients of the first canonical variable. Also for the muscle images, two of the most discriminant features were the GLCM correlation and contrast for both muscles. Furthermore, we analysed the texture features estimated on the images created using different dR values and using the beamforming methods as the independent group (**analysis A6**). The MANOVA was again applied, and in this case the d parameter was equal to 5 for both gastrocnemius and vastus lateralis muscle images. The features with the highest coefficient values of the first canonical variable are reported in Table 6. Fig. 8 shows the scatter plot of the first and second canonical variables of the MANOVA analysis among the dR values (Fig. 8 (A) and (B) refer to analysis A5) and beamforming methods (Fig. 8 (C) and (D) refer to analysis A6) for the gastrocnemius and vastus lateralis muscle images, respectively.

4. Discussion

In this study, we investigated texture features robustness across different ultrasound beamforming methods (DAS, F-DMAS, CF, GCF, PCF and SCF) and different dynamic range values (from 55 dB to 85 dB) for image visualization. Phantom images and two different kinds of *in vivo* muscle images (vastus lateralis and gastrocnemius muscles) were considered, and the variability of the texture features caused by the

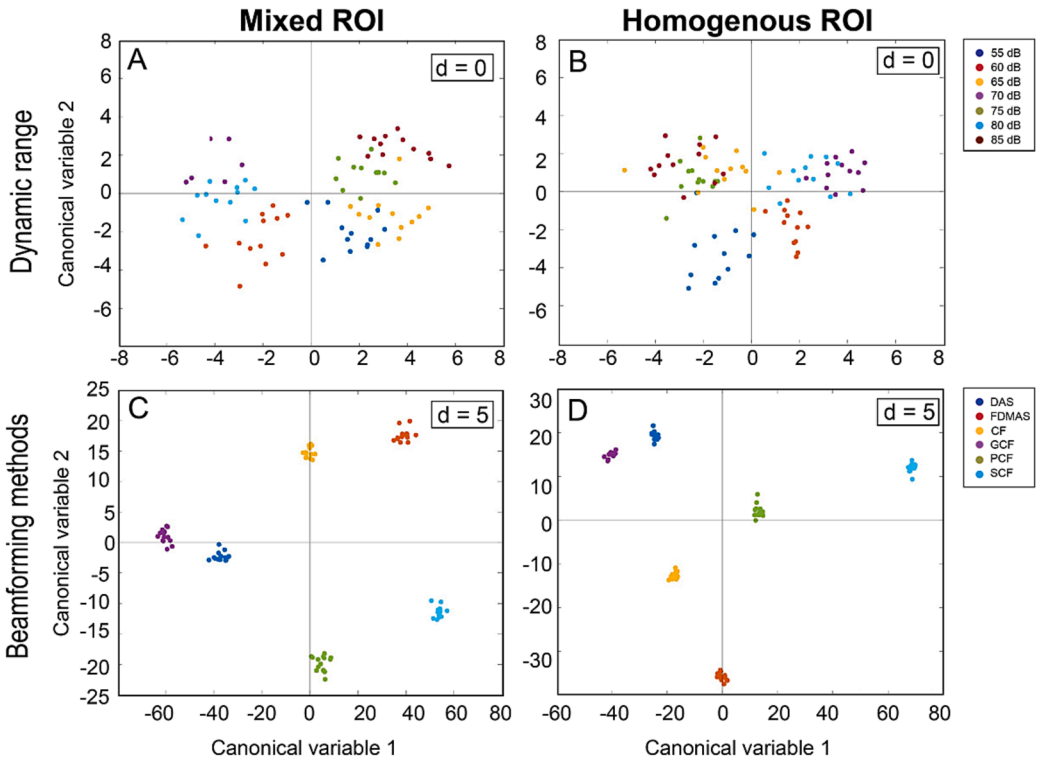

Fig. 7. The first and second canonical variables of texture features of the phantom images considering different ROIs: the combination of an anechoic and a uniform speckle region, and a reflector (A and C); the uniform-hyperechoic and uniform regions (B and D). (A) and (B) represent the results of MANOVA obtained with different beamforming methods using the dR values as the independent group (analysis A5), while (C) and (D) show the results of MANOVA obtained with different dR values using the beamforming method as the independent group (analysis A6).

Table 5
Analysis A5: Highest First Canonical Variable Coefficient Values.

	First	Second	Third	Fourth
Phantom *Homogeneous*	I_{cor} (90°)	I_{con} (0°)	I_{cor}(0°)	I_{con} (90°)
Phantom *Mixed*	I_{cor} (45°)	I_{cor} (0°)	*SRE* (45°)	I_{con} (0°)
Muscle *Gastrocnemius*	I_{cor} (0°)	I_{cor} (90°)	I_{con} (0°)	I_{cor} (0°)
Muscle *Vastus Lateralis*	I_{con} (0°)	I_{cor} (45°)	I_{con} (0°)	*RP* (0°)

Features with the highest coefficient values of the first canonical variable when considering the dR value as the independent group (analysis A5) for the phantom images (mixed and homogeneous ROIs) and muscle images (gastrocnemius and vastus lateralis). I_{cor} = GLCM correlation, I_{con} = GLCM contrast, SRE = short run emphasis, RP = run percentage. The considered angle is reported in parenthesis.

Table 6
Analysis A6: Highest First Canonical Variable Coefficient Values.

	First	Second	Third	Fourth
Phantom *Homogeneous*	I_{con} (0°)	I_{con} (90°)	*RP* (45°)	I_{con} (135°)
Phantom *Mixed*	I_{cor} (0°)	I_{cor} (135°)	*RP* (135°)	I_{con} (45°)
Muscle *Gastrocnemius*	I_{cor} (45°)	I_{cor} (135°)	I_{con} (90°)	I_{cor} (90°)
Muscle *Vastus Lateralis*	I_{con} (90°)	*RP*(90°)	I_{cor} (90°)	I_{cor} (135°)

Features with the highest coefficient values of the first canonical variable when considering the beamforming method as the independent group (analysis A6), for the phantom images (mixed and homogeneous ROIs) and muscle images (gastrocnemius and vastus lateralis). I_{cor} = GLCM correlation, I_{con} = GLCM contrast, RP = run percentage. The considered angle is reported in parenthesis.

change of the beamforming methods, dR values and the dimension/shape of the ROI selected for feature extraction was quantified. This investigation is intended to represent a step in motivating a broader look at the effects that various phases of the image formation process have on the extracted quantitative features. The texture within a B-mode ultrasound image has often been used to characterize tissue and, in particular, to discriminate between pathological and healthy tissues [48,49]. With this knowledge, the influence of the beamforming technique and of the dynamic range on the texture needs to be investigated. In a previous work [36], we analysed the robustness of the first and second order features estimated on images obtained with the six beamforming methods mentioned above, using only the coefficient of variation as a parameter of robustness. In this study, we expanded the analysis exploring the influence of the dimension/shape of the ROIs in which the features were estimated, and the beamforming methods and dR values used to create the final gray-level B-mode image. Furthermore, the images were acquired using two different ultrasound devices, ULA-OP and the Verasonics Vantage™ research ultrasound systems, making the obtained results more generalizable and applicable. Moreover, we also estimated higher-order features to improve the texture analysis, and included a more in-depth statistical analysis using ICC and MANOVA tests.

First of all, the ICC results show how the texture parameters were not greatly influenced by the ROI dimension or shape, both in the phantom and the muscle images (**analysis A1**). To be specific, the uniform areas of the phantom images show good robustness against variations in ROI size and shape, while mixed phantom and muscle regions show less robustness. This result can be explained by the fact that muscle zones are more similar to mixed phantom zones, as they contain areas of both higher and lower echogenicity which changes the patterns between pixels in a more drastic manner than when considering regions with a homogeneous echogenicity. In addition, by varying the size of the ROI, it is possible to select regions that vary their echogenicity and affect the texture features. Although the choice of ROI size is not a critical step in texture analysis, the location of the ROI is crucial. Indeed, when texture parameters are estimated to classify healthy tissues and pathological tissues, the correct positioning of the ROI, as well as its size, is of the uttermost importance, since it should be placed within the tissue to be investigated, without considering the different surrounding tissues. In our study, the size of the ROI was varied so that the region analysed always represented the tissue of interest.

Furthermore, another important aspect that was analysed here is the robustness of user-defined parameters of some renown coherence-based beamforming methods, i.e., GCF, PCF and SCF (**analysis A2**). In fact,

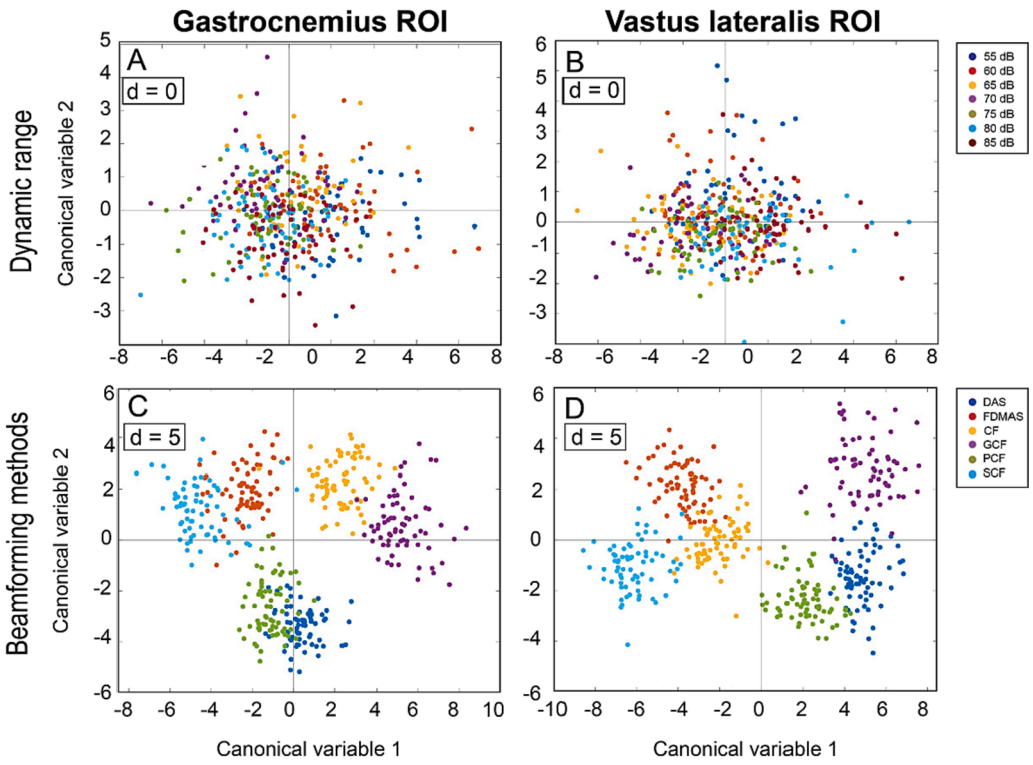

Fig. 8. The first and second canonical variables of texture features of the muscle images when considering the dR values as the independent group (A - B) (analysis A5), and the beamforming methods as the independent group (C - D) (analysis A6), for the gastrocnemius and vastus lateralis, respectively.

when employing these methods, it is necessary to set specific parameters (i.e., M_0, γ and p) to generate the beamformed data. Here we analysed the potential difference between the texture of the resulting ultrasound image when changing them, using the automatically determined dR, which permits to generate visually similar images when varying the parameters. Indeed, all ICC values estimated for the GCF, PCF and SCF methods are in a range of 0.63–0.99 for the phantom images and are higher than 0.83 for the muscle images, thus it can be concluded that generally there is a good repeatability of the texture in the obtained images, even when varying the values of these parameters, with lower ICC values achieved in the case of mixed phantom ROIs. However, it should be pointed out that to perform this analysis we used the automatically determined dR values. Hence, the choice of these parameters is also not a particularly critical step when focusing on the obtained ultrasound image texture if an automatically determined dR value is used to generate the final 8-bit gray-scale images, which likely makes them more similar visually.

An interesting finding from this study is the fact that the texture features are quite robust to changes in the dR when considering different dR values in the range [55; 85] dB for each beamforming method (**analysis A3**). In fact, the MANOVA analysis of the texture parameters obtained on all images (i.e., phantom and muscle) with just one beamforming method and using the dR value as the independent group gave a d value equal to zero for each single beamformer. This was also confirmed when separating the images into specific ROIs (i.e., mixed/homogeneous for the phantom and gastrocnemius/vastus lateralis for the muscle images) and applying the MANOVA analysis on the texture features computed on images obtained with the different beamforming methods and using the dR value as the independent group (**analysis A5**). This can be partially explained by the fact that the majority of considered texture features were higher-order features (5 first-order features vs 47 high-order features), that do not depend on the actual image intensity values (which are greatly affected by using different dynamic ranges) but rather on the patterns that may emerge from adjacent or close pixels, and on the fact that the human visual system can only distinguish between approximately fifty shades of gray, whereas the image 8-bit values are codified on 256 gray levels. Hence, although images obtained with the different dR values we considered are visually different, the patterns that emerge from adjacent pixels do not greatly vary. Indeed, the dynamic range value influences the visualization of the B-mode image but has no significant influence on the texture parameters, especially the higher-order features, as demonstrated also in [26,27]. Moreover, the higher-order texture parameters are not estimated directly from the B-mode image, but are extracted from the GLCM, RLM or LBP matrix, and aim to extract quantitative information from the texture of the image that are not necessarily easy to quantify with the naked human eye.

An intriguing finding of this study is that the MANOVA analysis shows that the beamforming methods can be distinguished using a combination of the texture features (i.e., canonical variables). This is observed in all MANOVA analyses that were done when using the beamforming method as the independent group, both when using the phantom and muscle images obtained with the automatic dR values together (**analysis A4**) and when using the seven different dR values in the range [55; 85] dB and separating the phantom and muscle images (**analysis A6**). Indeed, in all cases the dimension d is equal to 5 and the scatter plots of the first two canonical variables show how the beamforming techniques are in fact separated. This hints at the fact that a specific beamforming method could be more sensitive to changes in texture features due to a certain pathology (e.g., the change in texture observed in muscle ultrasound images in neuromuscular diseases [50] with respect to other beamforming techniques). An in-depth analysis of this is out-of-scope of the work presented here, but demonstrates the potential clinical applicability and impact of introducing new beamforming methods for ultrasound images in everyday clinical practice. The texture features that had the highest coefficient values of the first canonical variable were most often Haralick features, in particular the GLCM correlation and contrast at varying angles. These features analyse the number of times a specific intensity pattern between adjacent pixels is repeated. Since various beamforming methods typically aim to

increase both contrast and resolution in the obtained image, it can be expected that these texture parameters that specifically analyse a change in this pattern between adjacent pixels have an increased impact.

There are however some limitations in this study. Firstly, we analysed the texture of B-mode images created with DAS and some of the most commonly used coherence-based beamforming methods: F-DMAS, CF, GCF, PCF and SCF. However, adaptive beamformers have also been proposed for the improvement of resolution in ultrasound images, such as the minimum variance beamforming technique [51,52], and recently also deep learning methods have been used for beamforming, which could thus be included in future robustness analysis studies.

Moreover, the size of the analysed dataset is small, especially for phantom images, and this study was carried out considering only an interpixel distance equal to 1, and reducing the gray levels to 32 when computing the GLCM and RLM. Finally, the texture features computed on both the GLCM and RLM do not represent an exhaustive list of all available features [45]; their number was reduced here to include the most representative features for ultrasound images that have been used in previous studies [3,6,7,46]. This suggests that considering other texture features, and also different interpixel distances and different numbers of gray levels for the GLCM and RLM, could provide different results than those found in this study. In particular, other features could potentially show a distinction between texture features computed on images obtained with different dynamic range values using a MANOVA analysis, which was not found here. Still, it is important to underline that the findings of this work are in line with previous studies when considering differences between texture parameters and different dynamic range values [26,27]. On the other hand, as the MANOVA analysis showed that the beamforming methods can be distinguished using a combination of the considered texture features, it can be assumed that the inclusion of more texture features would reinforce the findings demonstrated here.

Furthermore, in this paper we did not study the potential capability of certain beamforming methods to discriminate better (or worse) between pathological and healthy images. This is in fact the final clinical goal and, as stated previously, the MANOVA results show a difference between the beamforming methods both in the phantom and muscle ultrasound images ($d = 5$), suggesting that a certain beamformer could potentially allow a better discrimination. This has yet to be analysed in depth and we are currently working on increasing the dataset to include such images. With an increase of the dataset size, our goal is also to evaluate the capability of using deep learning methods based on convolutional neural networks (CNNs) for the classification of the beamformed ultrasound images, to evaluate if a certain beamforming method produces images that are classified with a higher accuracy when compared to others.

5. Conclusions

In this work we presented a robustness analysis of texture features estimated on ultrasound B-mode images created with different beamforming techniques and dR values on phantom and *in vivo* muscle images. We analysed the texture features estimated from images acquired using two different ultrasound research scanners and demonstrated the high repeatability of the first and higher order texture features when varying the dynamic range used to generate the final 8-bit image. We further showed how a combination of texture features can distinguish beamforming methods through a MANOVA analysis, hinting at the potential future clinical applications and warranting further studies investigating the impact different beamforming methods have on tissue classification tasks.

Declaration of Competing Interest

The authors declare that they have no known competing financial interests or personal relationships that could have appeared to influence the work reported in this paper.

Data availability

The data that support the findings of this study are available from the corresponding author, [S. Seoni], upon reasonable request.

References

[1] A. Carovac, F. Smajlovic, dzelaludin Junuzovic, Application of Ultrasound in Medicine, Medicine Review | AIM 19 (3) (2011) 168–171, https://doi.org/10.5455/aim.2011.19.168-171.

[2] K.R. Erikson, F.J. Fry, J.P. Jones, Ultrasound in Medicine-A Review, IEEE Trans Sonics Ultrason 21 (3) (1974) 144–170, https://doi.org/10.1109/T-SU.1974.29810.

[3] F. Molinari, C. Caresio, U.R. Acharya, M.R.K. Mookiah, M.A. Minetto, Advances in Quantitative Muscle Ultrasonography Using Texture Analysis of Ultrasound Images, Ultrasound Med. Biol. 41 (9) (2015) 2520–2532, https://doi.org/10.1016/j.ultrasmedbio.2015.04.021.

[4] U. Rajendra Acharya, M. Muthu Rama Krishnan, L. Saba, F. Molinari, S. Guerriero, J.S. Suri, Ovarian tumor characterization using 3d ultrasound, Ovarian Neoplasm. Imag. (2013) 399–412, https://doi.org/10.1007/978-1-4614-8633-6_25.

[5] U.R. Acharya, O. Faust, S.V. Sree, F. Molinari, J.S. Suri, ThyroScreen system: High resolution ultrasound thyroid image characterization into benign and malignant classes using novel combination of texture and discrete wavelet transform, Comput. Methods Programs Biomed. 107 (2) (2012) 233–241, https://doi.org/10.1016/j.cmpb.2011.10.001.

[6] H.V. Cabral, K.M. Meiburger, L.F. de Oliveira, T.M. Vieira, Changes in supramaximal M-wave amplitude at different regions of biceps brachii following eccentric exercise of the elbow flexors, Eur. J. Appl. Physiol. 121 (1) (2021) 307–318, https://doi.org/10.1007/S00421-020-04520-4/FIGURES/6.

[7] U.R. Acharya, S.V. Sree, M.M. Krishnan, L. Saba, F. Molinari, S. Guerriero, J.S. Suri, Ovarian Tumor Characterization using 3D Ultrasound, Technol Cancer Res Treat. 11(6) 2012 Dec; 543-52. doi: 10.7785/tcrt.2012.500272. Epub 2012 Jul 10. PMID: 22775335.

[8] M. Pietikäinen, T. Ojala, Z. Xu, Rotation-invariant texture classification using feature distributions, Pattern Recogn. 33 (1) (2020) 43–52, https://doi.org/10.1016/S0031-3203(99)00032-1.

[9] T. Ojala, K. Valkealahti, E. Oja, M. Pietikäinen, Texture discrimination with multidimensional distributions of signed gray-level differences, Pattern Recogn. 34 (3) (2001) 727–739, https://doi.org/10.1016/S0031-3203(00)00010-8.

[10] U. Raghavendra, et al., Optimized multi-level elongated quinary patterns for the assessment of thyroid nodules in ultrasound images, Comput. Biol. Med. 95 (2018) 55–62, https://doi.org/10.1016/j.compbiomed.2018.02.002.

[11] M.M. Galloway, Texture analysis using gray level run lengths, Computer Graphics and Image Processing 4 (2) (1975) 172–179, https://doi.org/10.1016/s0146-664x(75)80008-6.

[12] T. Löfstedt, P. Brynolfsson, T. Asklund, T. Nyholm, A. Garpebring, Gray-level invariant Haralick texture features, PLoS One 14 (2) (2019) e0212110.

[13] U.R. Acharya, et al., Atherosclerotic Risk Stratification Strategy for Carotid Arteries Using Texture-Based Features, Ultrasound Med. Biol. 38 (6) (2012) 899–915, https://doi.org/10.1016/J.ULTRASMEDBIO.2012.01.015.

[14] U. Rajendra Acharya, S. Vinitha Sree, M. Muthu Rama Krishnan, F. Molinari, R. Garberoglio, J.S. Suri, Non-invasive automated 3D thyroid lesion classification in ultrasound: A class of ThyroScan^{TM} systems, Ultrasonics 52 (4) (2012) 508–520, https://doi.org/10.1016/j.ultras.2011.11.003.

[15] U. Raghavendra, et al., Fusion of spatial gray level dependency and fractal texture features for the characterization of thyroid lesions, Ultrasonics 77 (2017) 110–120, https://doi.org/10.1016/j.ultras.2017.02.003.

[16] W.K. Moon, I.L. Chen, J.M. Chang, S.U. Shin, C.M. Lo, R.F. Chang, The adaptive computer-aided diagnosis system based on tumor sizes for the classification of breast tumors detected at screening ultrasound, Ultrasonics 76 (2017) 70–77, https://doi.org/10.1016/j.ultras.2016.12.017.

[17] G. Matrone, A.S. Savoia, G. Caliano, G. Magenes, The delay multiply and sum beamforming algorithm in ultrasound B-mode medical imaging, IEEE Trans. Med. Imaging 34 (4) (2015) 940–949, https://doi.org/10.1109/TMI.2014.2371235.

[18] P.C. Li, M.L. Li, Adaptive imaging using the generalized coherence factor, IEEE Trans. Ultrason. Ferroelectr. Freq. Control 50 (2) (2003) 128–141, https://doi.org/10.1109/TUFFC.2003.1182117.

[19] J.F. Synnevåg, A. Austeng, S. Holm, Adaptive beamforming applied to medical ultrasound imaging, IEEE Trans. Ultrason. Ferroelectr. Freq. Control 54 (8) (2007) 1606–1613, https://doi.org/10.1109/TUFFC.2007.431.

[20] R. Paridar, B.M. Asl, Plane wave ultrasound imaging using compressive sensing and minimum variance beamforming, Ultrasonics 127 (2023), 106838, https://doi.org/10.1016/J.ULTRAS.2022.106838.

[21] C.C. Shen, P.Y. Hsieh, Ultrasound Baseband Delay-Multiply-and-Sum (BB-DMAS) nonlinear beamforming, Ultrasonics 96 (2019) 165–174, https://doi.org/10.1016/J.ULTRAS.2019.01.010.

[22] B. Luijten, et al., Adaptive Ultrasound Beamforming Using Deep Learning, IEEE Trans. Med. Imaging 39 (12) (2020) 3967–3978, https://doi.org/10.1109/TMI.2020.3008537.

[23] E. Mor, A. Bar-Hillel, A unified deep network for beamforming and speckle reduction in plane wave imaging: A simulation study, Ultrasonics 103 (2020), 106069, https://doi.org/10.1016/J.ULTRAS.2020.106069.
[24] W. Wang, Q. He, Z. Zhang, Z. Feng, Adaptive beamforming based on minimum variance (ABF-MV) using deep neural network for ultrafast ultrasound imaging, Ultrasonics 126 (2022), 106823, https://doi.org/10.1016/J.ULTRAS.2022.106823.
[25] A.A. Nair, K.N. Washington, T.D. Tran, A. Reiter, M.A. Lediju Bell, Deep Learning to Obtain Simultaneous Image and Segmentation Outputs from a Single Input of Raw Ultrasound Channel Data, IEEE Trans Ultrason Ferroelectr Freq Control 67 (12) (2020) 2493–2509, https://doi.org/10.1109/TUFFC.2020.2993779.
[26] M. A. Alqahtani, D. P. Coleman, N. D. Pugh, and L. D. M. Nokes, "Tissue characterization: Influence of ultrasound setting on texture features in vivo," *2010 International Conference on Medical Image Analysis and Clinical Application, MIACA 2010*, no. 4 cm, pp. 63–66, 2010, doi: 10.1109/MIACA.2010.5528423.
[27] G. Vara, A. Rustici, A. Sechi, C. Mosconi, V. Lucidi, R. Golfieri, Texture analysis on ultrasound: The effect of time gain compensation on histogram metrics and gray-level matrices, J Med Phys 45 (4) (2020) 249–255, https://doi.org/10.4103/jmp.JMP_82_20.
[28] O.M.H. Rindal, A. Austeng, A. Fatemi, A. Rodriguez-Molares, The Effect of Dynamic Range Alterations in the Estimation of Contrast, IEEE Trans. Ultrason. Ferroelectr. Freq. Control 66 (7) (2019) 1198–1208, https://doi.org/10.1109/TUFFC.2019.2911267.
[29] A. Rodriguez-Molares, et al., The Generalized Contrast-to-Noise Ratio: A Formal Definition for Lesion Detectability, IEEE Trans. Ultrason. Ferroelectr. Freq. Control 67 (4) (2020) 745–759, https://doi.org/10.1109/TUFFC.2019.2956855.
[30] Y. Lee, J. Kang, Y. Yoo, Automatic dynamic range adjustment for ultrasound B-mode imaging, Ultrasonics 56 (2015) 435–443, https://doi.org/10.1016/j.ultras.2014.09.012.
[31] S. Seoni, G. Matrone, K.M. Meiburger, Automatic Dynamic Range Estimation for Ultrasound Image Visualization and Processing, 2020 IEEE Int. Ultrason. Symp. (IUS), Las Vegas, NV, USA, 2020, pp. 1-4, doi: 10.1109/IUS46767.2020.9251470.
[32] A. Fatemi, Svein-Erik Måsøy, and Alfonso Rodriguez-Molares, "Row – Column-Based Coherence Imaging Using a 2-D Array Transducer : A Row-Based", IEEE Trans. Ultrason. Ferroelectr. Freq. Control 67 (11) (2020) 2303–2311.
[33] G. Matrone, A. Ramalli, J. D'Hooge, P. Tortoli, G. Magenes, A Comparison of Coherence-Based Beamforming Techniques in High-Frame-Rate Ultrasound Imaging with Multi-Line Transmission, IEEE Trans. Ultrason. Ferroelectr. Freq. Control 67 (2) (2020) 329–340, https://doi.org/10.1109/TUFFC.2019.2945365.
[34] N. Bottenus, B.C. Byram, D. Hyun, Histogram Matching for Visual Ultrasound Image Comparison, IEEE Trans. Ultrason. Ferroelectr. Freq. Control 68 (5) (2021) 1487–1495, https://doi.org/10.1109/TUFFC.2020.3035965.
[35] D. Hyun, G.B. Kim, N. Bottenus, J.J. Dahl, Ultrasound Lesion Detectability as a Distance Between Probability Measures, IEEE Trans. Ultrason. Ferroelectr. Freq. Control 69 (2) (2022) 732–743, https://doi.org/10.1109/TUFFC.2021.3138058.
[36] S. Seoni, G. Matrone, K.M. Meiburger, Robustness Analysis of Texture Features with Different Beamforming Techniques, 2020 IEEE Int. Ultrason. Symp. (IUS), Las Vegas, NV, USA, 2020, pp. 1-4, doi: 10.1109/IUS46767.2020.9251737.
[37] E. Boni, et al., A reconfigurable and programmable FPGA-based system for nonstandard ultrasound methods, IEEE Trans. Ultrason. Ferroelectr. Freq. Control 59 (7) (2012) 1378–1385, https://doi.org/10.1109/TUFFC.2012.2338.
[38] G. Matrone, A. Ramalli, Spatial coherence of backscattered signals in multi-line transmit ultrasound imaging and its effect on short-lag Filtered-Delay Multiply and Sum beamforming, Appl. Sci. (Switzerland) 8 (4) (2018) pp, https://doi.org/10.3390/app8040486.
[39] K. W. Hollman, K. W. Rigby, and M. O. Donnell, Coherence Factor, in 1999 IEEE Ultrasonics Symposium. Proceedings. International Symposium (Cat. No. 99CH37027), vol. 2, 1999, pp. 1257–1260.
[40] J. Camacho, M. Parrilla, C. Fritsch, Phase coherence imaging, IEEE Trans. Ultrason. Ferroelectr. Freq. Control 56 (5) (2009) 958–974, https://doi.org/10.1109/TUFFC.2009.1128.
[41] R.M. Haralick, I. Dinstein, K. Shanmugam, Textural Features for Image Classification, IEEE Trans. Syst. Man Cybern. SMC-3 (6) (1973) 610–621, https://doi.org/10.1109/TSMC.1973.4309314.
[42] U.R. Acharya, et al., Automated detection and classification of liver fibrosis stages using contourlet transform and nonlinear features, Comput. Methods Programs Biomed. 166 (2018) 91–98, https://doi.org/10.1016/j.cmpb.2018.10.006.
[43] O. Faust, et al., Comparative assessment of texture features for the identification of cancer in ultrasound images: a review, in: Biocybern Biomed Eng 38, PWN-Polish Scientific Publishers, 2018, pp. 275–296, https://doi.org/10.1016/j.bbe.2018.01.001.
[44] R. Obuchowicz, J. Kruszyńska, M. Strzelecki, Classifying median nerves in carpal tunnel syndrome: Ultrasound image analysis, Biocybern Biomed Eng 41 (2) (2021) 335–351, https://doi.org/10.1016/J.BBE.2021.02.011.
[45] M. Kociołek, M. Strzelecki, R. Obuchowicz, Does image normalization and intensity resolution impact texture classification? Comput. Med. Imaging Graph. 81 (2020), 101716 https://doi.org/10.1016/J.COMPMEDIMAG.2020.101716.
[46] K.M. Meiburger, et al., Quantitative Analysis of Patellar Tendon Abnormality in Asymptomatic Professional 'Pallapugno' Players: A Texture-Based Ultrasound Approach, Appl. Sci. 8 (5) (2018) 660, https://doi.org/10.3390/APP8050660.
[47] T.K. Koo, M.Y. Li, A Guideline of Selecting and Reporting Intraclass Correlation Coefficients for Reliability Research, J. Chiropr. Med. 15 (2) (2016) 155–163, https://doi.org/10.1016/j.jcm.2016.02.012.
[48] L. Niu, M. Qian, W. Yang, L. Meng, Y. Xiao, Surface Roughness Detection of Arteries via Texture Analysis of Ultrasound Images for Early Diagnosis of Atherosclerosis, PLoS One 8 (10) (2013) 76880, https://doi.org/10.1371/journal.pone.0076880.
[49] E. Bonet-Carne, et al., Quantitative ultrasound texture analysis of fetal lungs to predict neonatal respiratory morbidity, Ultrasound Obstet. Gynecol. 45 (2015) 427–433, https://doi.org/10.1002/uog.13441.
[50] F. Marzola, N. van Alfen, J. Doorduin, K.M. Meiburger, Deep learning segmentation of transverse musculoskeletal ultrasound images for neuromuscular disease assessment, Comput. Biol. Med. 135 (2021), 104623, https://doi.org/10.1016/j.compbiomed.2021.104623.
[51] J.F. Synnevåg, A. Austeng, S. Holm, Benefits of minimum-variance beamforming in medical ultrasound imaging, IEEE Trans. Ultrason. Ferroelectr. Freq. Control 56 (9) (2009) 1868–1879, https://doi.org/10.1109/TUFFC.2009.1263.
[52] R.G. Lorenz, S.P. Boyd, Robust Minimum Variance Beamforming, IEEE Trans. Sign. Process. 53 (5) (2005) pp, https://doi.org/10.1109/TSP.2005.845436.